small methods
www.small-methods.com

Fabrication of Na-Ion Full-Cells using Carbon-Coated $Na_3V_2(PO_4)_2O_2F$ Cathode with Conversion Type CuO Nanoparticles from Spent Li-Ion Batteries

*Krishnan Subramanyan, Manohar Akshay, Yun-Sung Lee, and Vanchiappan Aravindan**

Spent lithium-ion batteries (LIBs) offer immense potential in the form of resources such as Li, transition metals (Co, Ni, and Mn), graphite, and Cu, which can be recovered through suitable recycling procedures. The Cu-current collector is recovered from spent LIBs and converted as a copper oxide (CuO) anode for Na-ion batteries. The performance of CuO is evaluated with carboxymethyl cellulose (CMC) (CuO–C), and polyvinylidene fluoride (PVdF) (CuO–P) binders in CuO half-cell and CuO/carbon-coated $Na_3V_2(PO_4)_2O_2F$ (CuO/NVPOF) full–cell assemblies. The CuO–C half-cell displays superior electrochemical performance than CuO–P in terms of cycling and rate performance showing 88% more capacity. To study the stabilization and solid electrolyte interphase growth in CuO–C, an in situ impedance study is conducted. However, the full-cell, CuO–P/NVPOF displays better capacity retention during cycling with Coulombic efficiency >95% from the second cycle, whereas CuO-C/NVPOF could hardly maintain only >90%. For conversion type CuO, it is apparent that, though the CMC binder supports half-cell performance, the PVdF binder is suitable for the practical cell/full-cell configuration.

1. Introduction

The habit of reusing resources or ideas has been ingrained in human behavior due to multiple factors, most of which have been changed or even replaced with time. Though limited material availability might have been the prime intention of recycling, the onset of the Industrial Revolution enabled facile and cheap bulk production, which resulted in a use-and-throw mentality that led to ceaseless waste generation. Recycling has not entered the mainstream mainly due to the low return compared to the cost and workforce investment. The depletion of fossil fuel and the environmental issues caused by it has compelled us to focus on making the best out of renewable energy sources in terms of efficiently converting them into a usable form. The intermittent nature of such green sources demands an efficient energy storage device that is cheap, reliable, and, most importantly, employs greener technology. The sparse and widespread resources, combined with fluctuating supply chain of electrode raw materials, force us to rule out lithium-ion batteries (LIBs) as an option for such large-scale energy storage devices. For such big-scale storage applications, sodium-ion battery (SIB) will be an ideal candidate due to its enormous resource availability and even distribution across the globe[1,2]. Despite their widespread use, there is an acute deficiency in the LIB recycling technology and economic recovery of the current collector, transition metals, separator, graphite[3,4], and lithium metal that can be efficiently reused. Natarajan et al.[5] reported an economical process to recover separators from spent LIBs via simple washing and drying. Precious transition metals such as cobalt, manganese, and nickel have been successfully recovered from discarded LIBs using fatty-acid-based ionic liquid[6], metallurgical processes[7], chemical leaching[8], and more optimized techniques being developed to improve the percentage of recovery[9]. Meager works are available in recovering or reusing the current collector used in LIBs, and the copper current collector in the anode constitutes a noticeable share of the total price of the battery[10].

Herein, we report a simple yet efficient upcycling of used Cu current collector recovered from spent LIB into pristine CuO as an anode for SIB. Effective recycling of Cu current collectors can lead to a reduction in the production cost of active material since obtaining high-quality precursors can be avoided. A recent study shows that 1 sq. meter of high-quality Cu foil can cost up to $ 640[11]. Insertion type anodes have been a massive success due to their lesser volume expansion and stability[12]. However, due to their limited ion insertion capability, higher working potential, and sluggish kinetics, they are not ideal candidates as anodes[13]. At the same time, CuO is a conversion mechanism-based anode that can store two Na^+ ions during discharge, increasing the energy density[14,15]. CuO as anode material has been explored as CuO carbon composite[16,17] or CuO

K. Subramanyan, M. Akshay, V. Aravindan
Department of Chemistry
Indian Institute of Science Education and Research (IISER)
Tirupati 517507, India
E-mail: aravind_van@yahoo.com
Y.-S. Lee
School of Chemical Engineering
Chonnam National University
Gwang-ju 61186, Republic of Korea

The ORCID identification number(s) for the author(s) of this article can be found under https://doi.org/10.1002/smtd.202200257.

DOI: 10.1002/smtd.202200257

on copper[18,19] and pristine CuO with various morphologies. Xu et al.[20] reported a flower-like CuO anode, which exhibited excellent stability for LIBs, but the pristine material exhibited significant decay for SIB. Rath et al.[21] studied the CuO dependence of the performance of CuO on the morphology of the synthesized CuO. The group varied the structure-directing agent to synthesize morphologies such as nanorods, nanoellipsoids, and nanoflakes via hydrothermal self-assembly. We synthesize pristine CuO through a facile and highly scalable process in this work. Recycling will be meaningful and profitable only if performed on an industrial scale, making our synthesis highly reliable. Our process qualifies as an ideal recycling process since it does not involve any high cost, high purity chemicals, the requirement of an inert atmosphere, or sensitive techniques. Fan et al.[22] studied the performance dependence of CuO nanosheets on binders, viz. PVDF and CMC, where CMC was shown to exhibit better performance in all electrochemical tests. The FE-SEM image revealed that the CMC binder reduced the adverse effects on the electrode arising from the volume expansion due to the conversion reaction. This prompted us to fabricate half and full cells with both the binders in the CuO electrode to evaluate the change in performance if any. Electrochemical studies were performed on CuO half-cell and $CuO/Na_3V_2(PO_4)_2O_2F@C$ full-cell to assess the stability and capacity. The prime focus is on the performance of the pristine CuO without any additives, which makes ground for further research.

2. Results and Discussion

The X-ray diffraction (XRD) study was performed on the as-synthesized CuO particles, shown in **Figure 1**a. It confirms the formation of pure CuO without any noticeable impurity peaks, with two major peaks at ≈36° and ≈39° corresponding to the (–111) and (111) planes. CuO is seen to have a monoclinic structure with $a = 4.684$ Å, $b = 3.427$ Å, and $c = 5.132$ Å; $\alpha = \gamma = 90°$, $\beta = 99.51°$ belonging to the C12/c1 space group (DB card number: 01-077-7716). The average crystallite size of CuO was obtained to be 28.43 nm when calculated using the Debye-Scherrer formula,

$$D = \frac{0.9\,\lambda}{\beta \cos\theta} \tag{1}$$

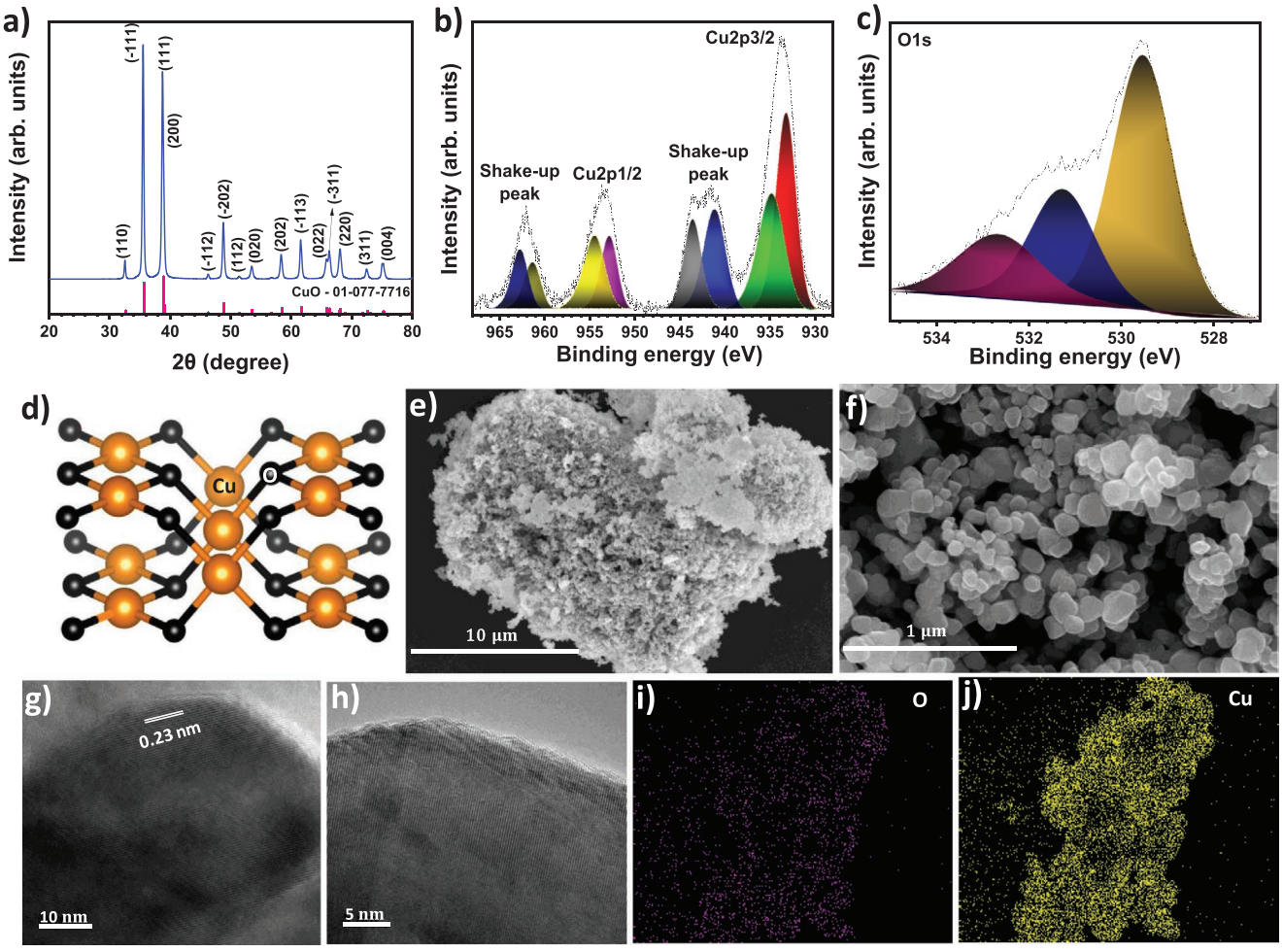

Figure 1. a) Powder XRD of CuO, high-resolution XPS spectra of b) Cu 2p, and c) O 1s, d) crystal structure of CuO, e,f) FE-SEM images of CuO at different magnifications, g,h) HRTEM images, and i,j) elemental distribution of CuO.

λ is the wavelength of the X-ray source used, β is the full width at half maximum of the peak in radians, θ is the Braggs angle in radians. The crystallographic structure of CuO is shown in Figure 1c. The field emission-scanning electron microscope (FE-SEM) analysis (Figure 1e–f) shows CuO particles of a few hundreds of nanometers (≈33 to ≈138 nm) in a dimension bound together forming clusters, and a high-resolution transmission electron microscope (HR-TEM) images (Figure 1g,h) show a regular periodic arrangement exhibiting excellent crystalline properties with a lattice plane separation of 2.3 å. This corresponds to the (200) plane of the crystal.

Figure 1b,c shows the X-ray photoelectron spectroscopy (XPS) analysis carried out to assert the chemical composition, purity, and oxidation state of CuO. The XPS survey spectrum of CuO is presented in Figure S1, Supporting Information. Two main factors that establish the presence of Cu^{2+}. a) There are strong shake-up satellites next to the Cu $2p_{3/2}$ peak and Cu $2p_{1/2}$ on the higher binding energy side. b) The Cu $2p_{3/2}$ peak is broad with a shift to the higher binding energy side[23]. The peak at ≈529.6 eV in the O 1s spectra corresponds to the Cu–O bonding. An EDS analysis was performed to study the bulk composition (Figure 1i,j), which shows the presence of only copper and oxygen with 76.4 and 26.3 wt.%, respectively. Additional elemental analysis and FE–SEM images have been included in Figure S2, Supporting Information.

2.1. Half-Cell Performance

Half-cells were fabricated with CuO electrodes consisting of PVDF and CMC binder and Na-metal counter/reference electrode. During the cathodic scan (discharge), there are three prominent peaks – 1.89, 0.5, and 0.1 V versus Na. These correspond to the CuO – Cu_{1-x}^{2+} Cu_x^{1+} O, $Cu_{1-x}^{2+}Cu_x^{1+}O_{1-x/2}$ – Cu_2O, and Cu_2O – Cu, transition respectively, and the end product being Cu^0 and Na_2O[16]. The whole reaction can be summarized as follows:

$$CuO + 2Na^+ + 2e^- \rightarrow Na_2O + Cu^0 \quad (2)$$

The oxidation peaks can be seen at 2.20 and 1.36 V versus Na, corresponding to the reverse reaction, *i.e.*, conversion of Cu^0 to Cu_2O and Cu_2O to CuO, respectively.

The initial cycle of CuO–P (P-stands for PVDF binder) half-cell CV shows a peak at 1.06 V versus Na, which does not appear in any further cycles (**Figure 2**a). This can be accredited to the decomposition of the organic electrolyte, which forms the solid electrolyte interface (SEI) layer that prevents further direct contact between the electrolyte and electrode. An additional irreversibility contribution also comes from the structural reorientation of CuO[16]. CuO–C (C-stands for CMC binder) half-cell also shows a minor peak at ≈1 V versus Na (Figure 2d) in the first cycle, which is not as evident as the peak in CuO–P half-cell. Nevertheless, the reduction peak for the CuO–C half-cell, close to 0.05 V versus Na, has a higher peak current than the CuO–P half-cell. Moreover, the initial Coulombic inefficiency (ICI) for CuO–P half-cell (63%) is higher than CuO–C half-cell (47%), and while the former takes 40 cycles to reach a Coulombic efficiency (CE) above 90%, the latter achieves this in the second cycle itself (Figure 2g–i). This is noticeable from the charge-discharge curves of the long-term cycling (Figure 2h–j) for the half-cells. It is also evident from the CV curves that there is negligible irreversibility in CuO–C half-cell for the second cycle, whereas CuO–P shows significant irreversibility even in the second cycle. The delay in attaining a higher CE in CuO–P can be interpreted as the inability of the PVDF binder to help in the formation of a stable and robust SEI layer[24]. Additional peaks appear in the anodic scan for CuO–P and CuO–C at 0.5 and 1.9 V versus Na in the second cycle and are seen to be present in all further cycles even at higher scan rates (Figure S3, Supporting Information). As the scan rate increases, it can be seen that the reduction peaks at 0.5 and 1.9 V versus Na become more prominent, with noticeable shifts in the peaks. While the cathodic peaks shift to higher potential, the anodic peaks shift to lower potential, except the peak at 0.1 V versus Na, which shifts to higher potential (Figure S3, Supporting Information).

The half-cells are also subjected to a rate performance test (Figures 2b,e,c,f), where the current rate has been varied from 25 to 1 A g^{-1} and back to 25 mA g^{-1} for CuO–P. We noticed that the performance of CuO–C was more elegant than CuO–P, attaining higher capacities for the same current rate and adjusting the current rates for CuO–C from 50 to 1.5 A g^{-1} and back to 50 mA g^{-1}. While CuO–P struggled at rates of 1 A g^{-1} with a discharge capacity of 86 mAh g^{-1}, CuO–C managed a whopping 157 mAh g^{-1}, 88% additional to CuO–P at a current density of 1 A g^{-1} and 128 mAh g^{-1}, 49% additional to CuO–P at a current density of 1.5 A g^{-1}. Since the rate performance was done without pre-conditioning, the initial low current cycles were seen to have irreversibility, which eventually disappeared at high currents. However, after the high current performance, CuO–C exhibited lower irreversibility than CuO–P.

The half-cell performances indicate dominance in performance for CuO–C over CuO–P and faster stabilization. The CMC binder has a crucial role in maintaining the whole structure of the electrode by preventing cracks in the electrode itself and preserving the electrode-current collector contact[22]. This implies that CMC is more effective than PVDF in curbing the volume expansion and associated issues arising from the conversion or alloying-based anodes [25]. From the charge-discharge curves, it was observed that CuO–C could attain a higher CE within two cycles, and it was associated with the SEI layer formation on the anode. To further understand this, we performed an in situ impedance study on CuO–C. The half-cell was initially discharged to 0.005 V versus Na from the open circuit potential and then charged to 3.00 V versus Na, followed by which two cycles of discharge-charge is performed from 0.005 to 3.00 V versus Na. Electrochemical impedance spectroscopy (EIS) (**Figure 3**) was performed at fixed voltages around anodic and cathodic peaks to observe the change in the impedance curve owing to (de)sodiation from the high frequency of 1 MHz to a low frequency of 10 mHz. An equivalent circuit for the Nyquist plots is given in Figure S6, Supporting Information. EIS has been proven to be one of the best non-destructive and non-invasive techniques to study the electrochemical reactions in a cell, such as an electrolyte solution resistance, charge-transfer resistance, and kinetics of the electrode, being a few of them[26,27]. The Nyquist plot is one of the forms of representation of EIS spectra, with a scale starting from the higher frequency to the

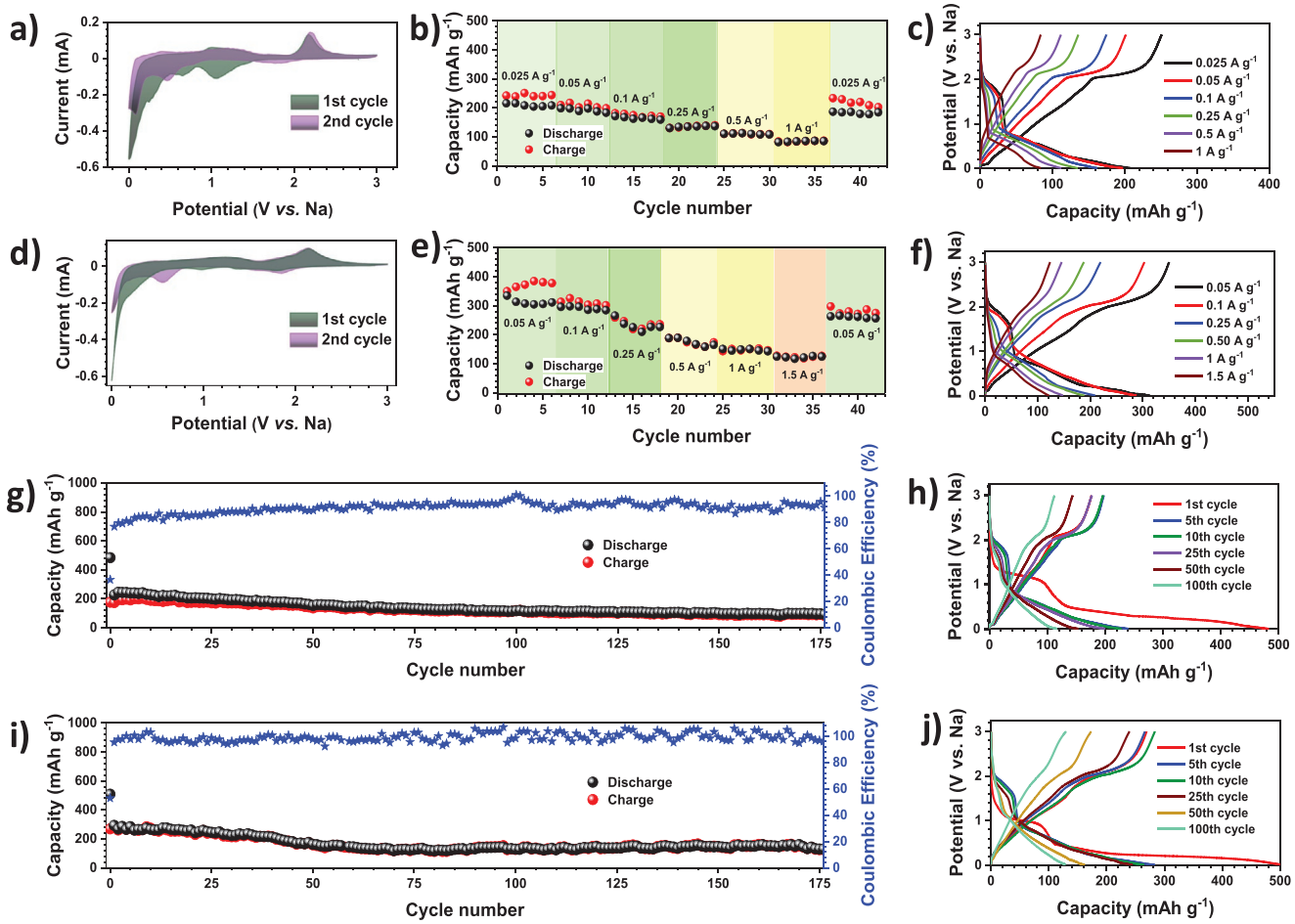

Figure 2. Cyclic voltammetry (CV), rate performance, and charge-discharge curves of rate performance for a–c) CuO–P, and d–f) CuO–C, long-term cycling, and charge-discharge curves at various cycles for g,h) CuO–P, and i,j) CuO–C. Long-term stability of CuO–P half-cell was evaluated at a current density of 50 mA g^{-1}, and CuO–C half-cell was evaluated at a current density of 100 mA g^{-1} to show its superior capacity and retention. The cells were cycled between 0.005 to 3.00 V versus Na.

lower frequency. EIS is an excellent technique to distinguish between resistive and capacitive contribution and hence ideal for studying the surface passivation film formation, which appears as the combination of capacitive and resistive contribution, forming a semi-circle in the mid-frequency region of a Nyquist plot. The spectra indicate the growth of a semi-circular portion of the EIS curve at a high frequency from the first cycle to the third cycle. There is a slight irregularity in the impedance values, predominantly seen in each EIS curve's charge-transfer resistance (R_{CT}), prominently in the first and second discharge cycles and the first charge cycle. There is a general trend for the EIS curves by the third cycle. In the third discharge, the R_{CT} is almost constant and starts to decrease when E_{cell} = 2.2 V versus Na, reaching a minimum at 1.5 V versus Na, further increasing to slightly higher R_{CT}, which is maintained till 0.005 V versus Na. The charged state when E_{cell} = 3.00 V versus Na was seen to have the most negligible impedance value. As the cell was being charged, R_{CT} remained almost constant, and around 2.2 V versus Na started decreasing, reaching the lowest value at the charged state. The R_{CT} at the end of the second charge is higher than the R_{CT} in the third charge, indicating that the layer formed becomes more conductive at the end of the third cycle. By the EIS study, it is clear that the formation of a stable and conductive SEI layer plays an imperative role in stabilizing CuO–C half-cell besides the buffering nature of the binder itself.

2.2. Full-Cell Performance

The performance of upcycled CuO was evaluated in balanced full-cell with CuO–P and CuO–C anodes and carbon-coated NVPOF cathode. The electrochemical characterization and the morphological studies of NVPOF were performed (Figures S4 & S5, Supporting Information). The as-synthesized material displayed a highly crystalline nature, evident from the sharp XRD peaks that match with previously reported work[28] and highly defined lattice planes illustrated in HR-TEM analysis (Figure S7, Supporting Information). NVPOF half-cell showed two anodic peaks (3.7 and 4.1 V versus Na) and three cathodic peaks (3.39, 3.54, and 3.92 V versus Na) in the initial cycle, which corresponds to the V^{4+} to V^{5+} and V^{5+} to V^{4+} redox reactions (Figure S8a, Supporting Information). The NVPOF half-cell exhibited a robust performance with capacity retention

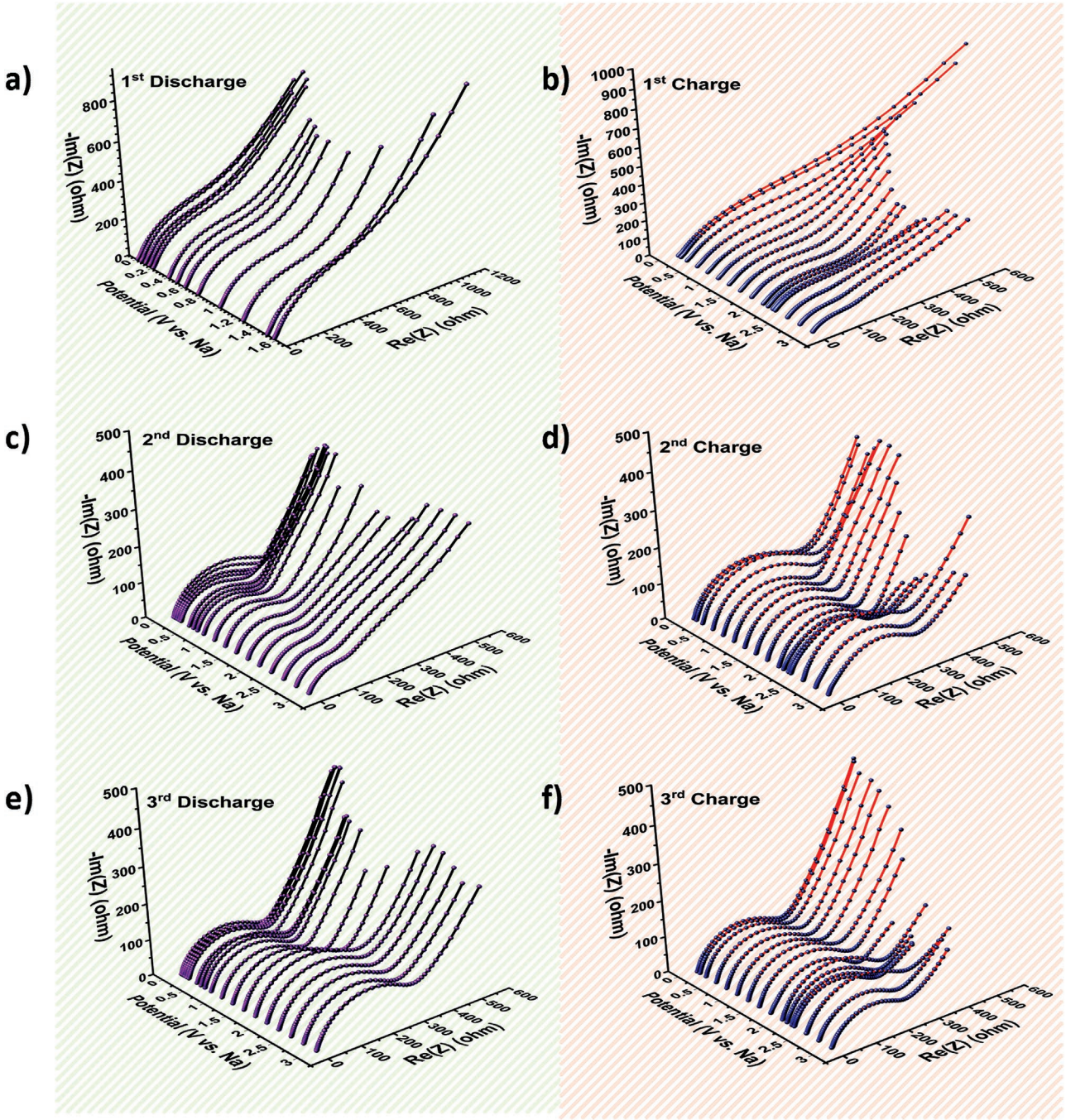

Figure 3. In situ EIS curves for CuO–C half-cell for a,b) 1st cycle, (c,d) 2nd cycle, and (e,f) 3rd cycle.

of 93% after 140 cycles at a current density of 50 mA g^{-1} (Figure S8e,f, Supporting Information). Thermogravimetric analysis (TGA) showed the presence of ≈7 wt.% of carbon in NVPOF (Figure S5c, Supporting Information). The high operating voltage, high capacity, and retention make it an ideal cathode material for the full-cell.

The electrochemical performance of the CuO–P/NVPOF full-cell is given in **Figures 4**a–d, and that of the CuO–C/NVPOF full-cell is given in Figures 4e–h. The first cycle of the CV for the full-cells exhibit almost similar anodic and cathodic peaks, except at high voltage values (Figure S9, Supporting Information). CuO–P/NVPOF shows a prominent peak for anodic and cathodic scans, which is also present for CuO–C/NVPOF but less apparent. It is discernable from the long-term performance at a current density of 0.25 A g^{-1} that CuO–C/NVPOF exhibits ≈1.5 times the initial capacity of that of CuO–P/NVPOF. However, as far retention is considered (after 100 cycles), CuO–P/NVPOF retains 49% of its initial discharge capacity, whereas CuO–C/NVPOF retains only 38% of its initial discharge capacity. This massive fade in the capacity of CuO–C/NVPOF

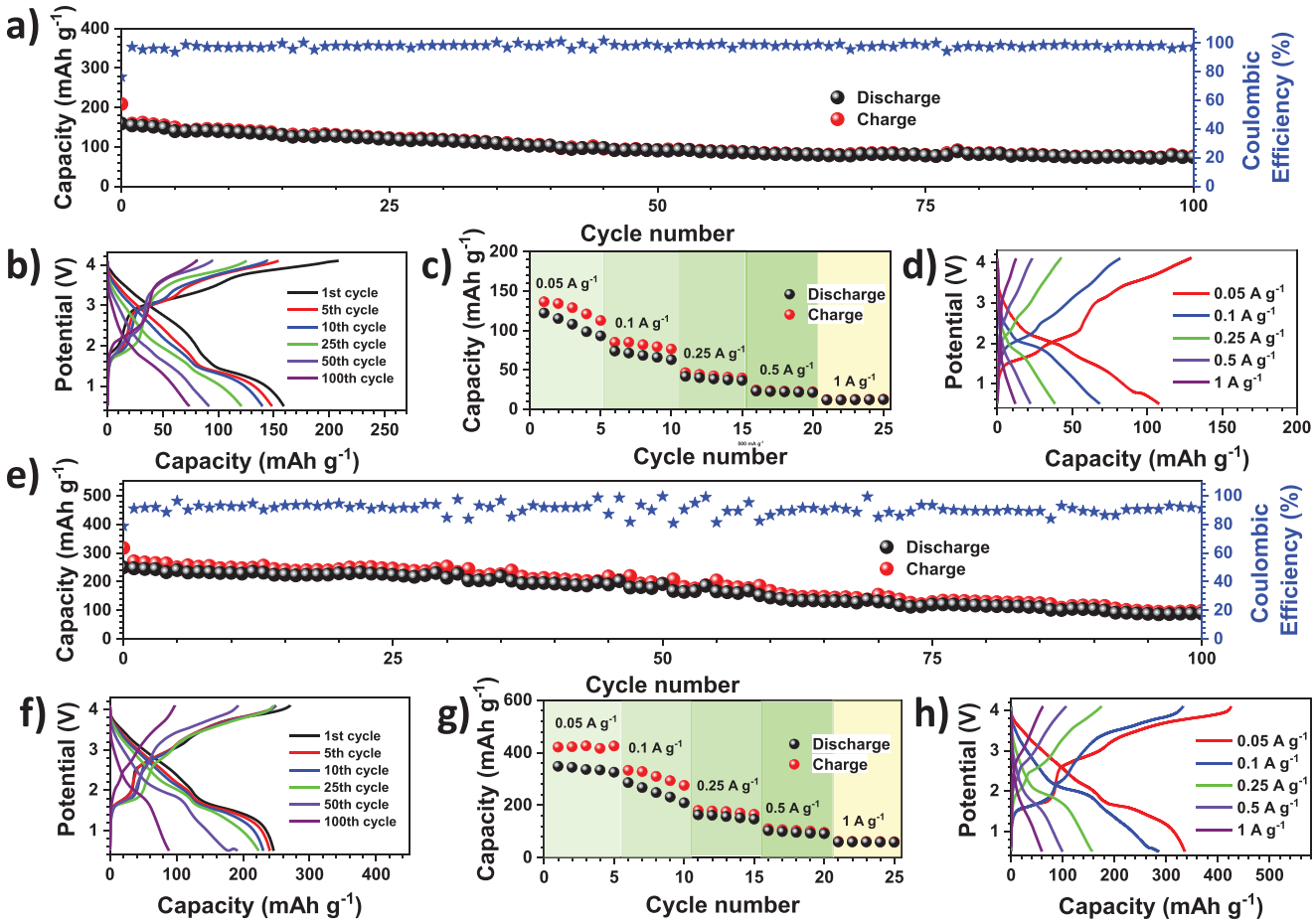

Figure 4. The electrochemical performance of a–d) CuO–P/NVPOF full-cell and e–h) CuO–C/NVPOF full-cell with long-term performance, charge-discharge curves of long-term performance, rate performance, and charge-discharge curves of rate performance, respectively. The long-term performance of both full-cells was evaluated at a current density of 250 mA g^{-1}. All the cells were evaluated from 4.1 to 0.5 V, and the capacity values were calculated from the anode mass loading.

can result from the poor CE, causing continuous irreversible consumption of Na^+ ions. Though CuO–C half-cell displayed excellent CE, the CuO–C/NVPOF full-cell exhibited an initial Coulombic efficiency (ICE) of 77%, with CE being maintained hardly above 90% in the following cycles. CuO–P/NVPOF displayed an ICE of 76%, with CE shooting up beyond 95% from the second cycle and managed to maintain it even after 100 cycles. There is a noticeable fading in the capacity of the full-cells with a prominent fade in CuO–C/NVPOF. The long-term performance of the full-cells with specific capacity determined by the anode and cathode active material masses is given in Figure S10, Supporting Information.

The rate performance showed that CuO–C/NVPOF exhibited a much better capacity at a current rate of 1 A g^{-1} than CuO–P/NVPOF, where the former had a capacity of 62 mAh g^{-1} and the latter with a capacity of 10 mAh g^1. The capacity and voltage in the full-cell were used to construct a Ragone plot for CuO–P/NVPOF and CuO–C/NVPOF, shown in **Figure 5**.

Both energy and power density has been calculated with the total mass of active material. The working voltage of CuO–C/NVPOF was found to be higher than CuO–P/NVPOF, but

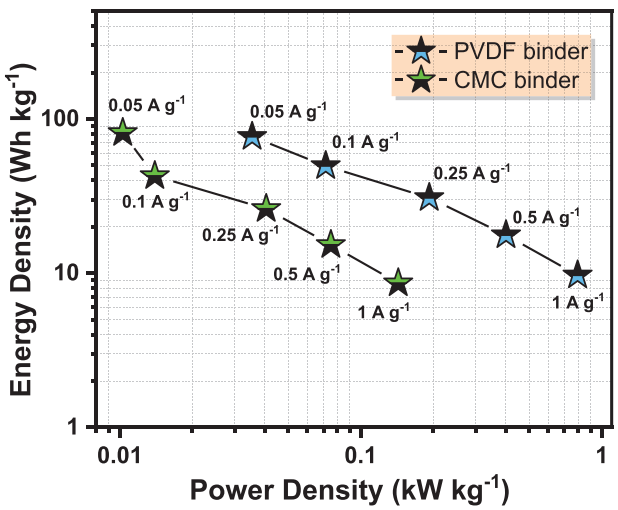

Figure 5. Ragone plots for CuO–P/NVPOF (represented as PVDF binder) and CuO–C/NVPOF (represented as CMC binder) based on the total mass of active materials (mass of CuO and mass of NVPOF).

except at a low current of 0.05 A g^{-1}, CuO–P/NVPOF was seen to dominate in both energy and power densities. At a current density of 0.05 A g^{-1}, CuO–C/NVPOF had a higher energy density value. These lower values of energy and power result from considering the total active material mass while constructing the Ragone plot since CuO–P/NVPOF has a lower total active material mass than CuO–C/NVPOF. This arises since a balanced full-cell was fabricated, where owing to the higher capacity of CuO–C, a higher active material mass of NVPOF has to be taken.

It is seen that both CuO–P and CuO–C-based half and full-cells have degradation and a CE which is not above 99%, which is essential to maintain the cycling for large number of cycles. This points out some recurring side reaction that consumes Na^+ from electrolyte[29] and cathode. Mitigating such factors can help in prolonging the life of the cell. Moreover, the synthesis mentioned in this work does not concentrate on morphology or particle size to promote performance. As future work, research to optimize the synthesis to obtain a morphology and particle size that maximize the performance has to be carried out. A more morphological and compositional analysis of the SEI layer has to be carried out, further establishing the performance difference between CMC and PVDF.

3. Conclusion

In this work, we developed a novel, efficient and scalable method to transform the copper current collector in spent LIBs to CuO anode in SIBs. The as-synthesized CuO was highly crystalline and was fabricated as electrodes with PVDF and CMC binders. CuO–C half-cell exhibited superior performance in terms of capacity, capacity retention, and rate performance over CuO–P half-cell. CuO–C half-cell displayed an additional 88% capacity than CuO–P at current density of 1 A g^{-1}. We observed that CuO–P half-cell struggled to attain a CE of over 90% and CuO–C half-cell attaining the same within the initial five cycles. Side reactions due to the improper formation of the SEI layer can cause this, and we performed an in-situ impedance study on CuO–C half-cell, which proved our assumption as it could form a proper SEI layer by the third cycle. The performance of CuO–P and CuO–C was further evaluated in full-cells which showed a stark variation from the performance of CuO–C in a half-cell. The CuO–C full-cell was unable to attain a high CE, which is crucial for the cell to achieve high cycling stability and further studies have to be performed to identify the root cause.

4. Experimental Section

CuO synthesis: CuO was synthesized through a simple precipitation reaction by recycling spent LIBs. Cu-foil was recovered from used mobile batteries through a reported procedure[30–32]. The battery leads were dipped in NaCl solution overnight to completely discharge it and then dried in an air oven at 75 °C. The battery was dismantled in a fume hood, and the Cu-foil obtained was immersed in distilled water and sonicated until loose graphite pieces came off. This was then dried at room temperature. It was immersed in dimethylformamide (DMF, Sigma Aldrich, anhydrous, 99.8%) overnight to ensure complete dissolution of the binder to separate all the graphite from the foil and dried at room temperature (**Scheme 1**). The Cu-foil was then cut into small pieces of approximately 5 mm, and 2 gm Cu-foil was dissolved in 20 mL of concentrated nitric acid (Sigma Aldrich, 70%) in a fume hood. After complete dissolution, 10 mL distilled water was added, and then NaOH solution was added dropwise until the solution became slightly basic. The precipitate was separated and washed with deionized water to remove any presence of sodium nitrate, followed by which it was dried in an oven at 75 °C. The as-obtained precipitate was heated at 500 °C for 2 h at a ramp rate of 5 °C min^{-1} and allowed to cool naturally to room temperature.

$Na_3V_2(PO_4)_2O_2F$@C (NVPOF) Synthesis: Carbon-coated NVPOF was synthesized via a simple hydrothermal technique according to a reported work[28]. Under constant stirring at 70 °C for 1 h, 1:3 molar

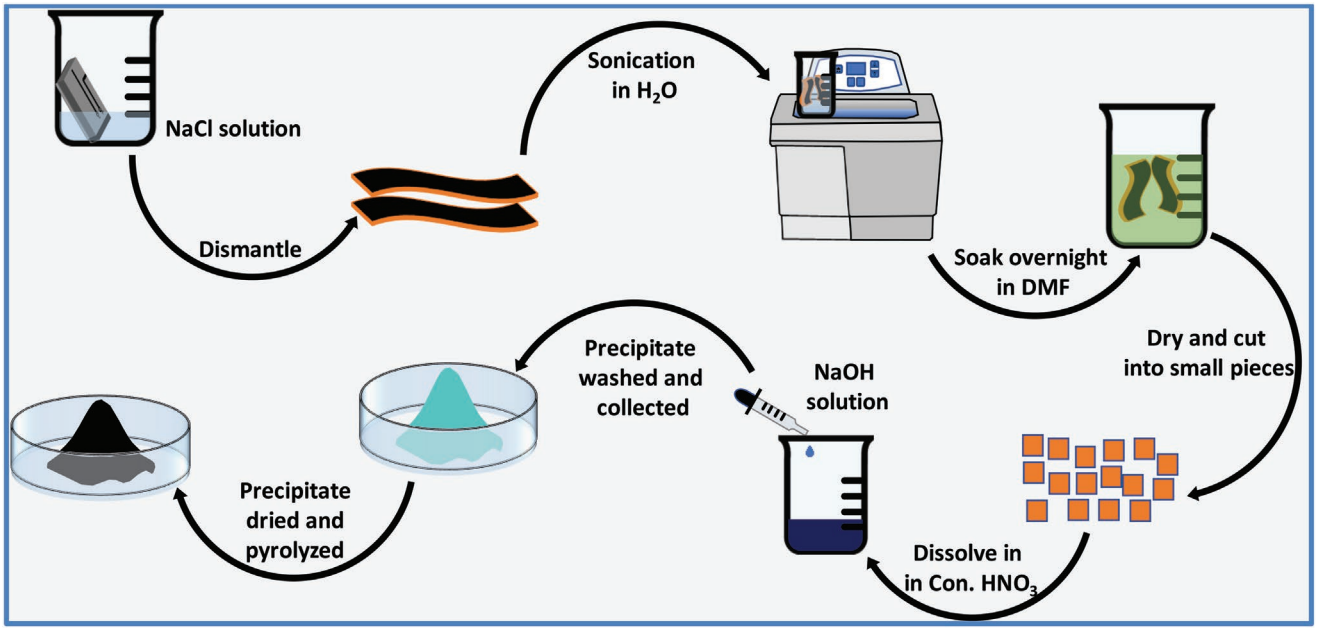

Scheme 1. Schematic illustration of the CuO nanoparticles from spent LIB current collectors.

ratio of V_2O_5 (Sigma Aldrich, >98%) and $H_2C_2O_4$ (Sigma Aldrich, >99%) was dissolved in distilled water to which a stoichiometric amount of $NH_4H_2PO_4$ (Sigma Aldrich, 98%), Na_2CO_3 (Sigma Aldrich, BioXtra, >99%), and NH_4F (Sigma Aldrich, 99.99%) were added. The above solution was transferred to a Teflon-lined autoclave, subjected to heating at 170 °C for 12 h, followed by natural cooling outside to obtain a light blue precipitate, which was collected and washed with distilled water several times and dried at 80 °C in a vacuum oven to obtain NVPOF.

Electrochemical Characterizations: CuO electrodes were cast on Cu-foil by doctor blade technique. CuO electrodes were fabricated with two binders, polyvinylidene fluoride (PVDF) and carboxymethyl cellulose (CMC). CuO electrodes with PVDF binder and CMC binder will be referred to as CuO–P and CuO–C, respectively. The active material (CuO), conductive additive (acetylene black), and binder ratio were set as 70:20:10 (wt.%). To fabricate CuO electrodes with PVDF binder, initially, PVDF was dissolved in 1-Methyl-2-pyrrolidinone (NMP, anhydrous, Sigma Aldrich, >99.5%) followed by the addition of acetylene black and CuO, which was kept under stirring overnight to form a homogenous slurry. This slurry was cast on Cu-foil using a doctor blade apparatus and kept for drying at 75 °C. After drying, it was pressed with a calendar roll and punched into electrodes of 12 mm diameter. CuO electrodes with CMC binder (Sigma Aldrich, average M_w ≈250000, degree of substitution 1.2) were fabricated similarly, but de-ionized water was used as the solvent to dissolve the binder. The areal mass loading of the active material for the anode was adjusted to be around 1.1 mg cm^{-2}. The NVPOF electrodes were fabricated with stainless steel mesh (Goodfellow, UK) as the current collector after matching capacity-mass loading of the anode. The detailed procedure for balanced full-cell fabrication is included in the supplementary information. For NVPOF half-cell, the mass of active material (NVPOF), conductive additive (acetylene black), and binder (teflonized acetylene black, TAB) were taken as 10 mg : 2 mg : 2 mg (areal mass loading of 6.5 mg cm^{-2}). Initially, a free-standing film is made in a mortar pestle with NVPOF, acetylene black, and TAB using ethanol solvent, which is pressed onto a stainless-steel mesh of 14 mm diameter in a pellet maker using a hydraulic press.

Half-cells and full-cell fabrication have been done in an inert glove box workstation (MBraun, Germany) with a glass microfiber separator (Whatman, cat no. 1825-047, UK) in CR2016 coin cell. Half-cells were fabricated with metallic sodium as the counter electrode. All the CuO electrodes were kept at 75 °C in a vacuum oven for a minimum of 4 h before cell fabrication. Prior to the fabrication of the full-cell, the CuO anode was subjected to pre-cycling for four cycles to mitigate the irreversibility. This was done in a CR2016 coin cell, which was de-crimped, and the electrode was carefully removed to be used as an anode in full-cell. Both full-cells and half-cells were fabricated with 1M $NaClO_4$ (Sigma Aldrich, >98%) in propylene carbonate (PC, anhydrous, Sigma Aldrich, >99.7%) and dimethyl carbonate (DMC, anhydrous, Sigma Aldrich, >99%) (1:1 vol.%) with 5 vol.% fluoroethylene carbonate (FEC, Sigma Aldrich, >99%) as additive. Electrochemical tests were performed in a BioLogic battery tester (BCS-805). The full-cell's electrochemical impedance spectroscopy and cyclic voltammetry were performed in Solartron electrochemical workstation (1470 E, UK).

Material Characterizations: The X-ray diffraction studies were carried out in Rigaku Smartlab automated multipurpose X-ray diffractometer at a scan rate of 0.5° min^{-1} with a monochromatic Cu Kα radiation of wavelength $\lambda = 1.5604$ Å. X-ray photoelectron spectroscopy (XPS, Multilab, 2000, UK) study was performed to analyze the surface composition of the material. The surface and internal structure were studied with field emission scanning electron microscopy (FE-SEM S-4700, Hitachi, Japan) and high-resolution transmission electron microscopy (HR-TEM, JEM-2000, EX-II, JEOL, Japan), respectively. Thermogravimetric analysis (TGA, Shimadzu, Japan) was done at 5 °C min^{-1} in air atmosphere.

Supporting Information

Supporting Information is available from the Wiley Online Library or from the author.

Acknowledgements

K.S. thanks the Department of Science & Technology (DST), Govt. of India for the financial support through INSPIRE fellowship (IF180157). YSL acknowledges the financial support from the National Research Foundation of Korea (NRF) grant funded by the Korean government (Ministry of Science, ICT & Future Planning) (No. 2019R1A4A2001527). VA acknowledges the financial support from DST and Science and Engineering Research Board through Swarnajayanti Fellowship (DST/SJF/PSA-02/2019-20 & SB/SJF/2020-21/12).

Conflict of Interest

The authors declare no conflict of interest.

Data Availability Statement

The data that support the findings of this study are available from the corresponding author upon reasonable request.

Keywords

binders, conversion type CuO, current collectors, polyanion $Na_3V_2(PO_4)_2O_2F$@C, pre-sodiation, sodium-ion batteries, spent Li-ion batteries

Received: March 1, 2022
Revised: March 16, 2022
Published online: April 24, 2022

[1] H. V. Ramasamy, N. P. Didwal, S. Sinha, V. Aravindan, J. Heo, C.-J. Park, Y.-S. Lee, *J. Colloid Interface Sci.* **2020**, *564*, 467.
[2] K. Subramanyan, V. Aravindan, *Chem* **2019**, *5*, 3096.
[3] S. Natarajan, V. Aravindan, *Adv. Energy Mater.* **2020**, *10*, 2002238.
[4] K. Subramanyan, S. Natarajan, Y. S. Lee, V. Aravindan, *Chem. Eng. J.* **2020**, *39*, *7*, 125472.
[5] S. Natarajan, K. Subramanyan, R. B. Dhanalakshmi, A. M. Stephan, V. Aravindan, *Batteries Supercaps* **2020**, *3*, 581.
[6] E. A. Othman, A. G. J. van der Ham, H. Miedema, S. R. A. Kersten, *Sep. Purif. Technol.* **2020**, *252*, 117435.
[7] L. Brückner, J. Frank, T. Elwert, *Metals* **2020**, *10*, 1107.
[8] W. Urbańska, *Minerals* **2020**, *10*, 555.
[9] J. C.-Y Jung, N Chow, D. D. Warkentin, K. Chen, M. Melashvili, Z. Meseldzija, P.-C. Sui, J. Zhang, *J. Electrochem. Soc.* **2021**, *167*, 160558.
[10] R. Schmuch, R. Wagner, G. Hörpel, T. Placke, M. Winter, *Nat. Energy* **2018**, *3*, 267.
[11] S. Natarajan, M. Akshay, V. Aravindan, *Adv. Sustainable Syst.* **2022**, *6*, 2100432.
[12] S. Natarajan, K. Subramanyan, V. Aravindan, *Small* **2019**, *15*, 1904484.
[13] L. Fang, N. Bahlawane, W. Sun, H. Pan, B. Xu, M. Bin; Yan, Y. Jiang, *Small* **2021**, *2101137*, 2101137.
[14] D. Mhamane, V. Aravindan, D. Taneja, A. Suryawanshi, O. Game, M. Srinivasan, S. Ogale, *Compos. Sci. Technol.* **2016**, *130*, 88.
[15] V. Aravindan, N. Arun, N. Shubha, J. Sundaramurthy, S. Madhavi, *Electrochim. Acta* **2016**, *215*, 647.
[16] Y. Lu, N. Zhang, Q. Zhao, J. Liang, J. Chen, *Nanoscale* **2015**, *7*, 2770.
[17] X. Wang, Y. Liu, Y. Wang, L. Jiao, *Small* **2016**, *12*, 4865.
[18] T. Zheng, G. Li, D. Li, X. Meng, *J. Nanopart. Res.* **2018**, *20*, 140.

[19] Y. Liu, Y. Qiao, W. Zhang, P. Hu, C. Chen, Z. Li, L. Yuan, X. Hu, Y. Huang, *J. Alloys Compd.* **2014**, *586*, 208.
[20] S. Xu, L. Lu, Q. Zhang, Q. Jiang, Z. Luo, S. Wang, G. Li, C. Feng, *J. Nanosci. Nanotechnol.* **2016**, *16*, 7655.
[21] P. C. Rath, J. Patra, D. Saikia, M. Mishra, C.-M. Tseng, J.-K. Chang, H.-M. Kao, *ACS Sustainable Chem. Eng.* **2018**, *6*, 10876.
[22] M. Fan, H. Yu, Y. Chen, *Mater. Technol.* **2017**, *32*, 598.
[23] S. K. Shinde, D. P. Dubal, G. S. Ghodake, V. J. Fulari, *RSC Adv.* **2015**, *5*, 4443.
[24] K. Subramanyan, Y.-S. Lee, V. Aravindan, *J. Colloid Interface Sci.* **2021**, *582*, 51.
[25] D. Bresser, D. Buchholz, A. Moretti, A. Varzi, S. Passerini, *Energy Environ. Sci.* **2018**, *11*, 3096.
[26] N. O. Laschuk, E. B. Easton, O. V. Zenkina, *RSC Adv.* **2021**, *11*, 27925.
[27] L. A. Middlemiss, A. J. R. Rennie, R. Sayers, A. R. West, *Energy Rep.* **2020**, *6*, 232.
[28] Z.-Y. Gu, J.-Z. Guo, Y. Yang, H.-Y. Yu, X.-T. Xi, X.-X. Zhao, H.-Y. Guan, X. He, X.-L. Wu, *Inorg. Chem. Front.* **2019**, *6*, 988.
[29] F. Klein, R. Pinedo, B. B. Berkes, J. Janek, *J. Phys. Chem. C* **2017**, *121*, 8679.
[30] S. Natarajan, D. S. Lakshmi, H. C. Bajaj, D. N. Srivastava, *J. Environ. Chem. Eng.* **2015**, *3*, 2538.
[31] S. Natarajan, S. R. Ede, H. C. Bajaj, S. Kundu, *Colloids Surf., A* **2018**, *543*, 98.
[32] S. Natarajan, H. C. Bajaj, *J. Environ. Chem. Eng.* **2016**, *4*, 4631.